



Article

Nonmetallic Active Sites on Nickel Phosphide in Oxygen Evolution Reaction

Pengfei Zhang [†], Hongmei Qiu [†], Huicong Li, Jiangang He, Yingying Xu ^{* } and Rongming Wang ^{* }

Beijing Advanced Innovation Center for Materials Genome Engineering, Beijing Key Laboratory for Magneto-Photoelectrical Composite and Interface Science, School of Mathematics and Physics, University of Science and Technology Beijing, Beijing 100083, China; zpf3516@163.com (P.Z.); hmqiu@ustb.edu.cn (H.Q.); 18166758766@163.com (H.L.); jghe2021@ustb.edu.cn (J.H.)

* Correspondence: xuyingying@ustb.edu.cn (Y.X.); rmwang@ustb.edu.cn (R.W.)

[†] These authors contributed equally to this work.

Abstract: Efficient and durable catalysts are crucial for the oxygen evolution reaction (OER). The discovery of the high OER catalytic activity in Ni₁₂P₅ has attracted a great deal of attention recently. Herein, the microscopic mechanism of OER on the surface of Ni₁₂P₅ is studied using density functional theory calculations (DFT) and ab initio molecular dynamics simulation (AIMD). Our results demonstrate that the H₂O molecule is preferentially adsorbed on the P atom instead of on the Ni atom, indicating that the nonmetallic P atom is the active site of the OER reaction. AIMD simulations show that the dissociation of H from the H₂O molecule takes place in steps; the hydrogen bond changes from O^a-H ··· O^b to O^a ··· H-O^b, then the hydrogen bond breaks and an H⁺ is dissociated. In the OER reaction on nickel phosphides, the rate-determining step is the formation of the OOH group and the overpotential of Ni₁₂P₅ is the lowest, thus showing enhanced catalytic activity over other nickel phosphides. Moreover, we found that the charge of Ni and P sites has a linear relationship with the adsorption energy of OH and O, which can be utilized to optimize the OER catalyst.

Keywords: Ni₁₂P₅; oxygen evolution reaction; adsorption energy; nonmetallic active site; ab initio molecular dynamics; density functional theory



Citation: Zhang, P.; Qiu, H.; Li, H.; He, J.; Xu, Y.; Wang, R. Nonmetallic Active Sites on Nickel Phosphide in Oxygen Evolution Reaction. *Nanomaterials* **2022**, *12*, 1130. <https://doi.org/10.3390/nano12071130>

Academic Editors: Xiaoyan Li, Kai Liu and Yinghui Sun

Received: 10 March 2022

Accepted: 26 March 2022

Published: 29 March 2022

Publisher's Note: MDPI stays neutral with regard to jurisdictional claims in published maps and institutional affiliations.



Copyright: © 2022 by the authors. Licensee MDPI, Basel, Switzerland. This article is an open access article distributed under the terms and conditions of the Creative Commons Attribution (CC BY) license (<https://creativecommons.org/licenses/by/4.0/>).

1. Introduction

The increasing global energy demand and environmental pollution make it imperative to develop more efficient and sustainable energy conversion technologies [1–4]. Hydrogen is one of the most plentiful elements in the universe and the most efficient green fuel. However, most hydrogen on earth only exists in water molecules. Electrocatalytic water splitting is one of the most promising technologies for hydrogen generation [5–7]. At present, the efficiency of electrocatalytic water splitting is too low to meet the requirements of large-scale applications. Electrocatalytic water splitting consists of two half-reactions, the oxygen evolution reaction (OER) and the hydrogen evolution reaction (HER) [8]. The OER involves the transfer of four electrons, which usually has a relatively high overpotential and constrains the efficiency of water splitting; therefore, more efficient catalysts for OER have to be carefully designed in order to accelerate the reaction [9,10].

On the other hand, at present the most efficient electrocatalysts for OER reactions are Ir/Ru/Pt-based noble metals or their oxides [11–13]. However, the high cost of these noble metal-containing electrocatalysts significantly impedes their large-scale application in industrial production. Therefore, the development of high-performance and low-cost catalysts is highly desirable. Recently, cheap transition metal oxides [14,15], phosphides [16–19], nitrides [20], sulfides [21–24], carbides [25], etc., have been studied as emerging electrocatalysts, and many show excellent OER catalytic activity.

Among these, nickel phosphides (Ni₂P, Ni₃P, Ni₅P₄, Ni₁₂P₅, etc.) have attracted a great deal of attention recently [26–31]. In particular, high OER catalytic activity has been

reported in Ni₁₂P₅. Menezes demonstrated that Ni₁₂P₅ shows stronger OER performance compared to Ni₂P [31]. Xu et al. found that Au/Ni₁₂P₅ core/shell nanoparticles (NPs) show high OER catalytic activity and that a synergetic effect exists in the single crystalline core/shell structure [32]. The OER activity of Ni₂P has been extensively studied theoretically [33–35]. However, there are few theoretical studies on the OER mechanism of Ni₁₂P₅, especially studies combining theory with molecular dynamics. In a previous study, Wen et al. verified that the rate-determining step for the OER of Ni₁₂P₅ is the formation of the OOH group, and the energy barrier is 1.58 eV; however, the OER active site of Ni₁₂P₅ has not been thoroughly studied [36].

Density functional theory (DFT) has been widely used to analyze the electrochemical water splitting process and study the catalytic activity of OER [37–40]. Ab initio molecular dynamics (AIMD) provides microscopic insights into the structural and dynamical properties of aqueous solutions, which serves as a perfect supplement to experimental studies [41–44]. In order to provide a basis for understanding the catalytic mechanism of Ni₁₂P₅, in this work we used AIMD and DFT calculations to study the OER catalytic process on nickel phosphides. It was found that the dissociative adsorption of H₂O is at the nonmetallic P site, not the Ni site. In addition, we found that the adsorption energies of OH and O are linearly correlated with the amount of charge at the adsorption sites. Furthermore, our calculations show that the overpotential of Ni₁₂P₅ is lower than in other nickel phosphides, which explains its excellent OER catalytic activity. This study unveils the microscopic mechanism of OER on the surface of Ni₁₂P₅ and provides a general picture of charge transfer on nickel phosphides, which can benefit catalyst design in the future.

2. Computational Details

2.1. Static DFT Calculations

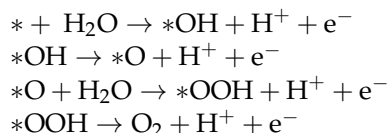
In the static calculations, the spin-polarized DFT calculations were performed using the Vienna Ab initio Simulation Package (VASP) [45,46]. The generalized gradient approximation (GGA) of the Perdew–Burke–Ernzerhof (PBE) functional was applied to optimize the geometric structures [47]. The interactions between the ions and valence electrons were described using the Projector Augmented Wave (PAW) method [48]. The slab structure was relaxed, with fixed in-plane lattice constants along with the bottom layer until the force on each atom was less than 0.01 eV/Å. The convergence criterion of the total energy for all the calculations was set as 1×10^{-5} eV, and the *k*-point sampling within the Brillouin zone for different structures is shown in Table S1. The plane wave basis was adopted for all of the calculations, with a cutoff energy of 400 eV.

The adsorption energy was calculated using the following equation:

$$E_{\text{ads}}(X) = E_{*+X} - E_* - E_X \quad (1)$$

where E_{*+X} is the DFT total energy of the slab with X species adsorbed on the surface and E_X and E_* are the total energies of X species and the slab with a clean surface, respectively.

An OER consists of four basic reaction steps, with each step involving one electron transfer and one proton removal [39]:



in which * denotes a surface site and *X represents an adsorbed X intermediate on the surface. The reaction free energy for each step is calculated using

$$\Delta G = \Delta E + \Delta E_{\text{ZPE}} - T\Delta S \quad (2)$$

where ΔE , ΔE_{ZPE} , and ΔS are the ground state energies calculated by DFT, zero-point energy, and the entropy correction values, respectively [39,49,50]. Additional computational details are described in the Supporting Information.

2.2. AIMD Simulations

AIMD simulations were carried out using the CP2K package with the canonical NVT ensemble, employing Nosé–Hoover thermostats with a target temperature of 300 K [51]. The MD time step was set to 1.0 fs. The DFT in CP2K/Quickstep is based on the mixed Gaussian Plane Wave (GPW) [52]. The matrix diagonalization method was used to optimize the wave function. The double- ζ Gaussian basis set with one set of polarization functions (DZVP) was used [53], and the plane wave basis was set with an energy cutoff of 350 Ry. The O 2s2p, P 3s3p, and Ni 3s3p3d4s were treated as valence electrons and the other electrons were placed in the cores utilizing Goedecker–Teter–Hutter (GTH) pseudopotentials [54,55]. The Perdew–Burke–Ernzerhof (PBE) [56] exchange–correlation functional and the Grimme D3 method [57] of correction to the van der Waals interaction were adopted.

The surface of Ni₁₂P₅ (001) was simulated by a p (2×2) supercell with four atomic layers. The vacuum space between the slab and its periodic image was 15 Å; therefore, the size of the Ni₁₂P₅ (001) supercell was $17.2 \times 17.2 \times 22.9$ Å³. Ni₁₂P₅ (001)/H₂O was simulated using the explicit solvent model. Water solution was added above the surfaces of Ni₁₂P₅ (001) with thickness of 11 Å and volumetric density of 1 g/mL. The Ni₁₂P₅ (001)/H₂O model contains 144 Ni atoms, 60 P atoms, and 100 H₂O molecules.

3. Results and Discussion

3.1. Stability of Ni₁₂P₅ Surface

Ni₁₂P₅ crystallizes in a body-centered tetragonal structure with a space group of I4/m, as shown in Figure 1a. The P atom has two Wyckoff positions in Ni₁₂P₅; one is located at the center of a cube formed by the 8-Ni-atom, and the other is located in the center of the polyhedron with the 10-Ni-atom (Figure 1b). The fully relaxed lattice constants of bulk Ni₁₂P₅ are $a = b = 8.644$ Å and $c = 5.051$ Å, which are within 0.3% of the error when compared with the experimental data ($a = b = 8.646$ Å and $c = 5.070$ Å, JCPDS 89-3697).

To determine the most stable surface of Ni₁₂P₅ for catalysis study, we calculated the surface energies of several different low-index surfaces using DFT (Figures S1 and S2). According to Reuter and Scheffler's surface energy calculation method [58], the surface energy of Ni₁₂P₅ is defined as

$$E_{\text{surf}} = \left[\frac{1}{2A} E_{\text{slab}} - n_{\text{Ni}} E_{\text{Ni bulk}} - n_{\text{P}} E_{\text{P bulk}} - \frac{E_{f, \text{Ni}_{12}\text{P}_5}}{12} + \Delta\mu_{\text{P}} \left(\frac{5n_{\text{Ni}}}{12} - n_{\text{P}} \right) \right]$$

where E_{slab} is the total energy of the surface model, $E_{\text{Ni bulk}}$ and $E_{\text{P bulk}}$ are the total energies per atom of metal Ni and black P, $E_{f, \text{Ni}_{12}\text{P}_5}$ is the formation energy of Ni₁₂P₅, n_{Ni} and n_{P} are the numbers of Ni and P atoms in the surface model, respectively, $\Delta\mu_{\text{P}}$ is the chemical potential of P, and A is the surface area of the surface model.

Five low-index surfaces of Ni₁₂P₅, namely (001), (100), (110), (101), and (111), are considered in this work; the calculated results are shown in Figure 1c. Within the thermodynamically stable district (-1.2 eV $<$ $\Delta\mu_{\text{P}}$ $<$ -0.4 eV) of Ni₁₂P₅ [59], the surface energies of these surfaces follow the order (001) $<$ (100) $<$ (110) $<$ (101) $<$ (111). Surface (001) has the lowest E_{surf} , and hence is the most stable surface. Therefore, we focus on surface (001) in this work.

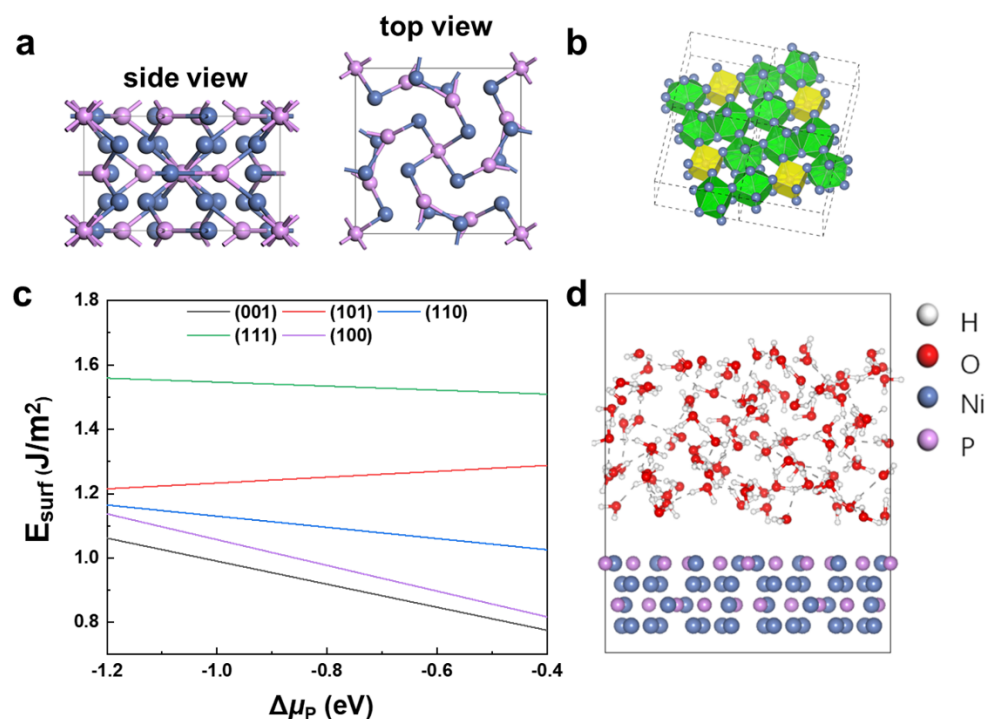


Figure 1. (a) Crystal structure of Ni₁₂P₅. (b) Equivalent sites of P ions. Yellow is the P-centered cube with 8-Ni-atom and green is P-centered polyhedron with 10-Ni-atom. (c) Surface energies of low-index surfaces (001), (101), (110), (100), and (111) as a function of P chemical potential ($\Delta\mu_P$). (d) Ni₁₂P₅ (001)/H₂O model. The white, red, purple, and blue spheres represent H, O, P, and Ni, respectively.

3.2. The Adsorption and Dissociation of H₂O on the Surface of Ni₁₂P₅

AIMD simulations with an explicit solvent model (Figure 1d) were performed for several Ni₁₂P₅ (001)/H₂O models, with random distribution of initial water molecules in NVT ensemble at 300 K. Movies of the reaction trajectories are provided in the Supporting Information (Movie 1). The explicit solvent model can capture the interactions among H₂O molecules in aqueous solution, and is therefore able to describe the dynamic process of H₂O molecules at the surface more accurately.

Individual snapshots from the MD trajectory of H₂O at the Ni₁₂P₅ (001)/H₂O are displayed in Figure 2a. During the entire simulation process, an H₂O molecule is first adsorbed on the top of a P atom on the surface of Ni₁₂P₅ (001) and then an H⁺ is dissociated into the solution, which corresponds to the reaction of $^*\text{OH}_2 \rightarrow ^*\text{OH} + \text{H}^+ + \text{e}^-$. The H₂O dissociation process can be studied in detail by monitoring the distances between the involved atoms as a function of the simulation time. As shown in Figure 2b, we can see that the whole process can be divided into the following periods (where O^a is the O atom in the adsorbed H₂O and ^{*}OH and O^b is the O atom in another H₂O in solution):

(a) Period I: 0–320 fs; H₂O approaches the surface of Ni₁₂P₅ (001).

At first, due to thermal motion at room temperature, an H₂O molecule in the aqueous solution moves towards the Ni₁₂P₅ (001) surface, which corresponds to the decreasing P–O^a distance. While the P–O^a distance approaches ~ 2.00 Å, the H–O^a bond length of the H₂O molecule maintains ~ 0.98 Å, which corresponds to the H–O bond length of H₂O gas. Meanwhile, a hydrogen bond, O^a–H \cdots O^b (2.65 Å, \cdots denotes a hydrogen bond), is formed.

(b) Period II: 320–375 fs. H₂O is adsorbed and H dissociation starts; the hydrogen bond transforms.

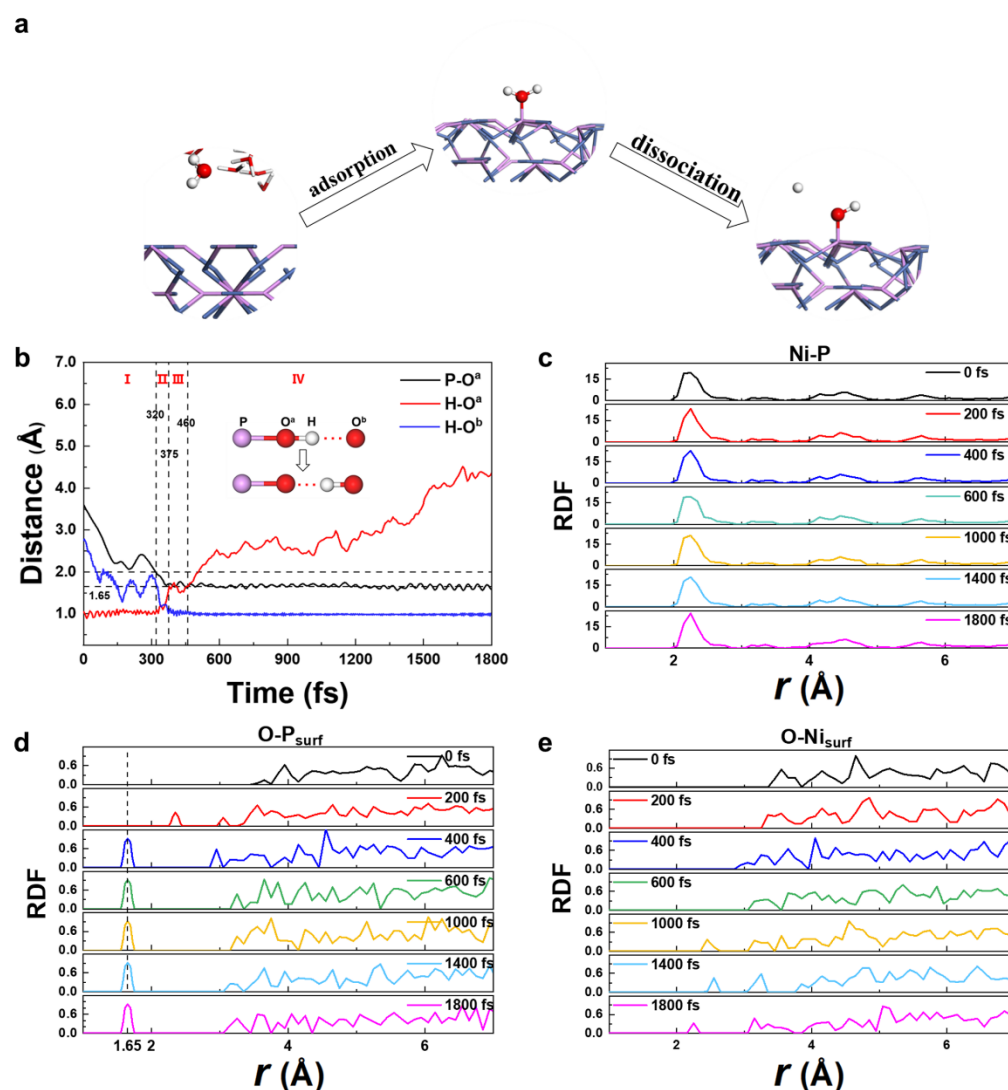


Figure 2. (a) Selected snapshots of the AIMD trajectory for Ni₁₂P₅ (001)/H₂O at 300 K. The white, red, purple, and blue spheres represent H, O, P, and Ni, respectively. (b) The time evolution of the key bond distances during the AIMD simulation. The black line is the bond distance between the P-O^a. The red line is the bond distance between the H-O^a. The blue line is the bond distance between the H-O^b. H is the dissociated H⁺, O^a is the O atom in *OH; O^b is the O atom in another H₂O. Radial distribution function (RDF) changes over time: (c) among Ni and P atom; (d) P atoms on the surface and O atom in H₂O; (e) Ni atoms on the surface and the O atom in H₂O.

With the P-O^a distance decreasing, one H⁺ of the H₂O^a molecules becomes more and more active and begins to dissociate from the H₂O^a molecule. At 375 fs, the P-O^a distance decreases to 1.65 Å, which is close to the P-O σ bond length (1.61 Å) in P₂O₅, indicating that the P-O^a bond is formed. Meanwhile, one of the H-O^a bond lengths increases from 0.98 Å to 1.60 Å, and the dissociated H⁺ forms H₃O⁺ with another H₂O molecule. In this process, the hydrogen bond transforms from P-O^a-H ··· O^b to P-O^a ··· H-O^b; the hydrogen bonds length are 2.65 Å.

(c) Period III: 375–460 fs; the metastable state, while P-O^a is connected with an H through the hydrogen bond, P-O^a ··· H-O^b.

The O^a atom remains bonded with the P atom, and the P-O^a bond length is shortened to 1.65 Å. The hydrogen bond P-O^a ··· H-O^b remains stable.

(d) Period IV: After 460 fs; the breaking of the hydrogen-bond, H⁺ completely leaves the surface.

The hydrogen bond $\text{P-O}^{\text{a}} \cdots \text{H-O}^{\text{b}}$ starts to break, and $\text{H}_3\text{O}^{\text{b}+}$ leaves the surface site.

The similar processes of H_2O dissociative adsorption from the two other AIMD simulations with different initial water molecules are shown in Figures S3 and S4. There are two rapid processes: First, the process of P-O^{a} bond shortening from 2.00 Å to 1.65 Å in Period II takes around 50–75 fs, which is the H_2O chemical adsorption on Ni_{12}P_5 (001) surface. Second, the dissociation of the hydrogen bond from the H_2O molecule (the $\text{O}^{\text{a}}\text{-H}$ bond length increases from 1.60 Å to over 2.00 Å) in Period IV takes ~50 fs experimentally, Z.-H. Loh et al. found the time to form OH and H_3O^+ from the ionized H_2O^+ and H_2O is about 46 fs [60], which is consistent with what we found from AIMD simulation. Because the energy required to break O-H bond is much larger than to break a hydrogen bond, the step-by-step dissociation of H^+ with catalyst is thermodynamically more favorable.

On the other side, the metastable state with partially dissociated H and hydrogen-bond $\text{P-O}^{\text{a}} \cdots \text{H-O}^{\text{b}}$ in Period III can persist as long as 1 ps (Figure S3). A hydrogen bond widely exists between two H_2O molecules (about ~0.21 eV/bond in H_2O [61]) in solutions and is the main intermolecular interaction in the liquid [62,63]. In the Period III, the state with hydrogen bond structure may be metastable.

We further verified these results with radial distribution functions (RDF). As can be seen from the RDF plot of Ni and P atoms in Figure 2c, the distances of Ni-P do not change significantly, which indicates that the Ni_{12}P_5 (001) surface is stable in aqueous solution. Figure 2d shows the RDF between O atoms in H_2O and one P atom at the Ni_{12}P_5 (001) surface. At 0 fs the P-O distance is around 4 Å, which corresponds to the start point, when H_2O molecules are not adsorbed on the surface yet. At 200 fs, a peak appears at 2.45 Å, indicating that H_2O is moving towards the Ni_{12}P_5 surface. At 400 fs, the peak shifts to 1.65 Å. From 400 fs to 1800 fs, the peak keeps its shape and position at 1.65 Å, indicating a stable P-O bond has been formed and the H_2O is adsorbed on the surface of Ni_{12}P_5 (001). Figure 2e shows the RDF of the O and Ni atoms on the surficial layer. We found no any peak in the RDF within the range of $r < 3$ Å, which means no H_2O molecules were adsorbed to Ni atoms. After 1000 fs there is a small peak appearing in the range of 2–2.5 Å; it can be inferred that after *OH is bonded to the P site, the H_2O molecule in solution may approach the Ni site during thermal motion. The time evolution of the Ni-O distance is detailed in Figure S5. No stable Ni-O bond was found in any of our simulations.

From the above discussion, the adsorption and dissociation process of H_2O on the surface of Ni_{12}P_5 is captured in the AIMD simulations. In this process, the transformation and fracture of the hydrogen bond plays an important role. It should be noted that the H_2O molecule prefers to adsorb on the nonmetal P site instead of the metal Ni site, which is uncommon in transition metal compounds [37–39], and will be discussed in the next section.

3.3. Nonmetallic P Atoms as Active Sites

Transition metals with partially filled d orbitals are generally the active catalytic sites in OER [16,17,21,64]. Recently, it has been reported that nonmetal atoms may become the active sites for catalytic reactions in theoretical studies [63–65]. For example, Legare et al. found that B atoms could be active sites in nitrogen reduction [65]. Deng et al. pointed out that in Pt-loaded MoS_2 the active site are the surface S atoms directly connected to Pt [66]. Huang et al. showed that in $\text{Ni-N}_4\text{-Cs}$, OH and O tend to adsorb on the second adjacent C atom, while OOH and OO are formed on the central Ni atom [67]. It was pointed that the interaction between the central metal atom and its adjacent coordination atoms can tune the catalytic performance from the aspects of electronic structure, spatial coordination, etc. Thus, the coordinated nonmetal atoms may act as the active sites for the catalytic processes [68].

The stabilities of adsorption groups at the P site on Ni_{12}P_5 surface were further examined. An adsorbed group (OH or O) was set on the top of the P and Ni sites, respectively, of the Ni_{12}P_5 (001) surface and the relative energies of these two configurations were computed by using more accurate static DFT calculations. As can be seen from Figure 3, the total energy of the system decreased from Ni^*OH ($^*\text{O}$) to P^*OH ($^*\text{O}$), and the energy

difference (ΔE) between these two configurations was -1.15 eV (-2.56 eV), which indicates that OH (O) prefers to adsorb on the P atom rather than the Ni of the Ni_{12}P_5 (001) surface. In addition, our AIMD simulations (Movies 2–5) show that the adsorbed OH on the P atom remains stable, while OH adsorbed on Ni moves to its adjacent P atom in 450 fs (Figure 3a). Similarly, the adsorbed O on Ni moves to the nearby P atom in 150 fs (Figure 3b), and the adsorbed O on P atom remains stable.

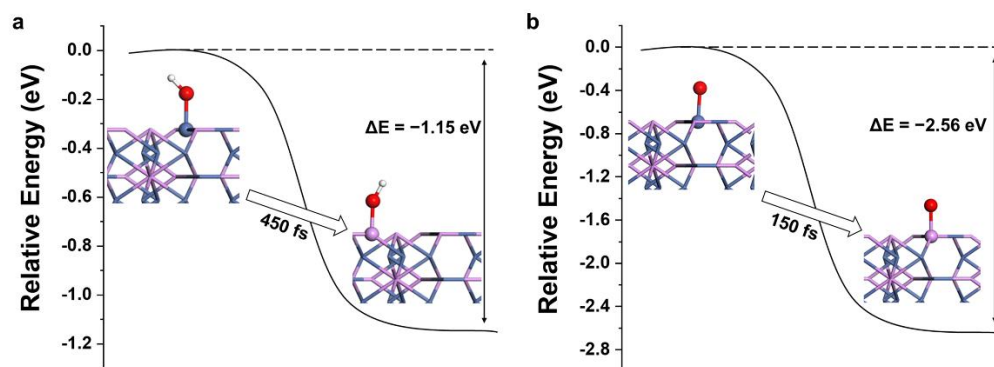


Figure 3. Relative energy distributions for different products on Ni_{12}P_5 (001) surface: (a) $\text{Ni}^*\text{OH} \rightarrow \text{P}^*\text{OH}$ (b) $\text{Ni}^*\text{O} \rightarrow \text{P}^*\text{O}$. The white, red, purple, and blue spheres represent H, O, P, and Ni, respectively.

As discussed above, we found that the OER active site on the surface of Ni_{12}P_5 is the nonmetal P site; we discuss the active sites and catalytic activity of OER in several nickel phosphides in Section 3.4. In the catalytic process, the electronic structure of the nonmetallic P active sites may be affected by coordinated Ni atoms, which is detailed in Section 3.5.

3.4. Active Site of OER in Nickel Phosphides

In this subsection, we investigate the electronic properties of active sites and the catalytic activities of several nickel phosphides using the static DFT method. The surface electrostatic potential of Ni_2P , Ni_{12}P_5 , Ni_5P_2 , Ni_3P , and NiO are shown in Figure 4a–e. The typical OER electrocatalyst NiO , the active site of which is Ni, is used as a reference. The Ni–O bond on NiO is mainly ionic and the electrostatic potential varies sharply. Compared with NiO , the electrostatic potential fluctuations of the Ni_2P , Ni_{12}P_5 , Ni_5P_2 and Ni_3P surfaces are smaller. Due to the small electronegativity difference between P and Ni, P is only slightly negatively charged, while Ni is slightly positively charged; therefore, the Ni–P bond is mainly covalent.

Different surface structures that satisfy the nickel and phosphorus stoichiometric ratio of the compound were selected in order to calculate the adsorption energies of OH and O (Figures S6–S13). As shown in Figure 4f, the adsorption energies of OH (O) at the P site are always lower than that of Ni on the Ni_2P , Ni_{12}P_5 , Ni_5P_2 and Ni_3P surfaces, indicating that the active catalytic sites on these nickel phosphides are P atoms. Moreover, the adsorption energies of OH and O on the surface of Ni_{12}P_5 are the lowest among all the studied nickel phosphides in this work. We noted that P has more suspended bonds than Ni atoms on the exposed surfaces of Ni_2P , Ni_{12}P_5 , Ni_5P_2 , and Ni_3P (Table S2). In general, step, apex, and highly unsaturated coordination atoms usually tend to be active sites of OER [69,70], which may explain why H_2O tends to adsorb on P site.

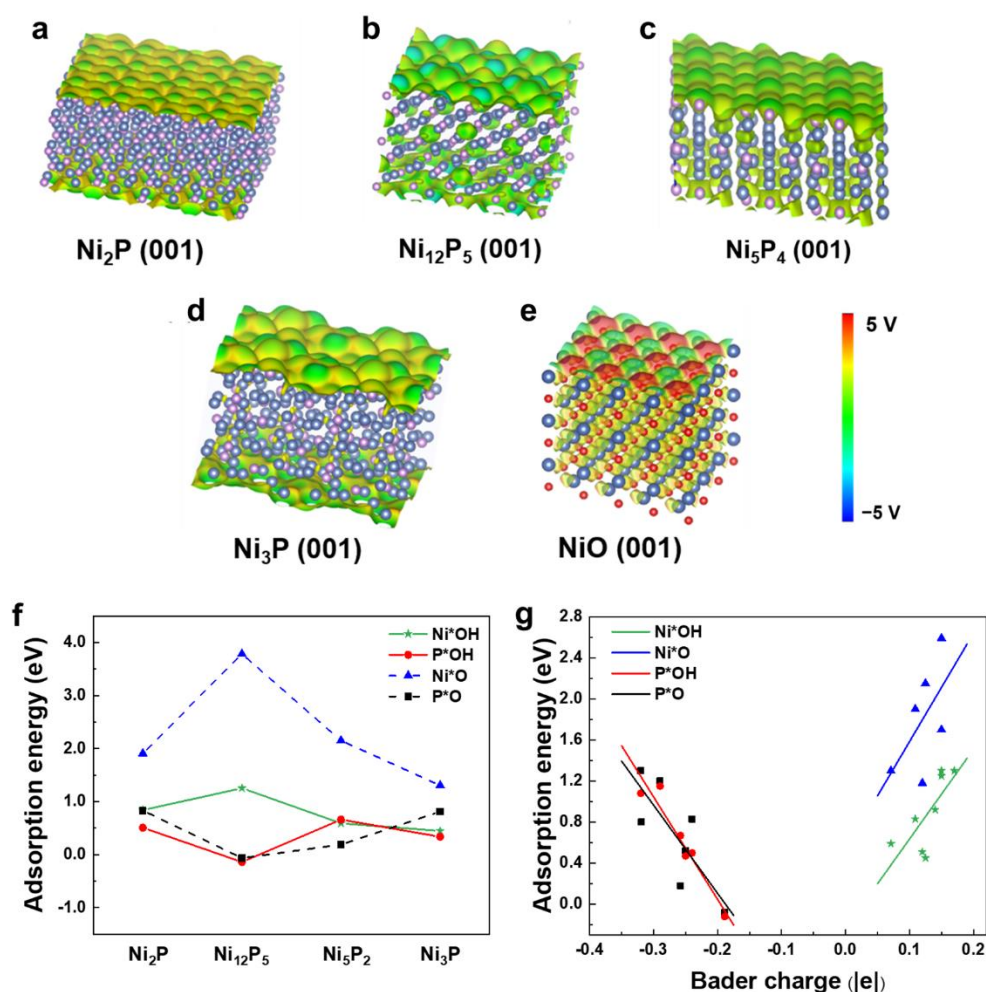


Figure 4. Surface electrostatic potential: (a) Ni₂P (001), (b) Ni₁₂P₅ (001), (c) Ni₅P₂ (001), (d) Ni₃P (001), and (e) NiO (001). The isosurface value is set to 0.2 e/Å³. (f) Adsorption energies of OH and O adsorbents on the surfaces of Ni₂P (001), Ni₁₂P₅ (001), Ni₅P₂ (001), and Ni₃P (001). (g) The relationship between adsorption energy (OH and O) and Bader charge of the atom (Ni or P) bonded with adsorbents.

Previous studies have shown that large charge transfers between active sites and adsorption groups usually correspond to lower adsorption energies. To unveil the underlying mechanism of the adsorption behavior of OH and O on nickel phosphides, we calculated the amount of charge transfer at the sites on the nickel phosphide surface when OH (or O) was adsorbed. As can be seen from Table 1, the electrons in P and Ni transfer to the adsorbed O atom, which is more electronegative. We found that the transferred charge is strongly correlated with adsorption energy, i.e., larger charge transfers between OH or O and adsorption sites are correlated with lower adsorption energy in the corresponding adsorption structure. The larger transferred charge indicates low charge transfer resistance between the adsorption site and the OH and O groups, which can promote the adsorption of these groups, thus showing excellent performance [71–73].

Table 1. The amount of charge transfer of OH or O after adsorption, along with adsorption energies for nickel phosphide.

	Charge/e ⁻	E _{ads} /eV		Charge/e ⁻	E _{ads} /eV
*OH	0.37	2.54	*O	0.15	1.24
	0.85	1.71		0.21	0.92
	0.89	1.42		0.21	0.82
	0.91	1.31		0.40	0.69
	0.94	0.51		0.43	0.50
	0.95	0.53		0.44	0.45

(* denotes a surface site)

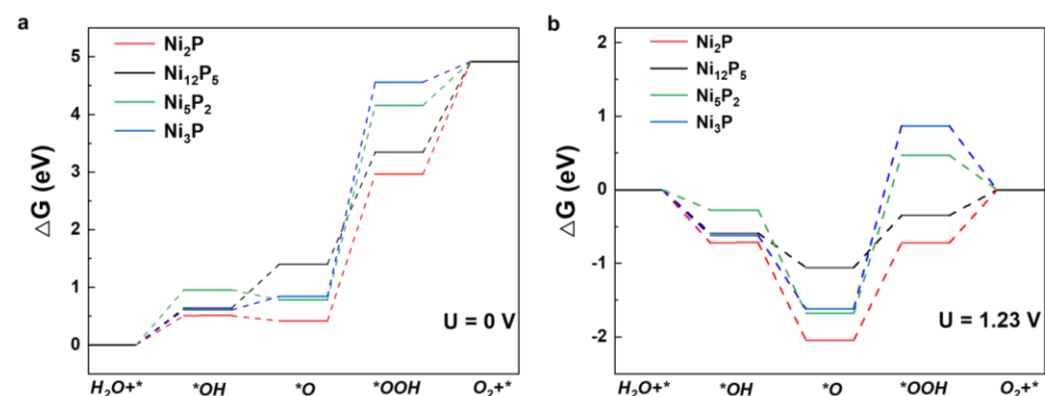
Because the adsorption energies of OH and O are related to the amount of transferred charge, there may be a correlation between the adsorption energy and the amount of charge at the adsorption site. Therefore, we calculated the charge of the Ni and P sites of the clear nickel phosphide surface (Figure 4g). It was found that the amount of charge at the active site has a linear relationship with the adsorption energy. As shown in Table 2, when the charge of the P atom is in the range of -0.4 to -0.15 |e|, the adsorption energy of OH or O decreases with the increase of charge. When the charge of Ni is in the range of 0.05 to 0.2 |e|, the adsorption energy of OH or O is directly proportional to the charge.

Table 2. Formulas corresponding to different structures.

Structures	Formulas
Ni*OH	$E_{ads} = 8.72q - 0.24$
Ni*O	$E_{ads} = 10.55q + 0.53$
P*OH	$E_{ads} = -9.97q - 1.95$
P*O	$E_{ads} = -8.58q - 1.61$

(* denotes a surface site).

As shown in Figure 5a, the Gibbs energies corresponding to each reaction step show an upward trend under standard conditions ($U = 0$ V), meaning that extra energy is needed to promote the reaction. Figure 5b shows that the electronic transfer step from *O to *OOH has the highest free energy gradient, indicating that it is the rate-determining step (RDS) for the OER process. Obviously, the third step energy barrier for Ni₁₂P₅ is 0.71 eV, which is lower than for the Ni₂P (1.32 eV), Ni₅P₂ (2.15 eV), and Ni₃P (2.49 eV) structures, indicating that Ni₁₂P₅ has best OER catalytic activity; this is consistent with the experimental results (Table S3).

**Figure 5.** Gibbs energy diagram of OER intermediates on the catalyst surfaces at electrode potentials (a) $U = 0$ V and (b) $U = 1.23$ V.

3.5. Charge Distribution at Ni₁₂P₅ (001)/H₂O

In the OER catalytic process, the electronic structure of the nonmetallic P active sites may be affected by coordinated Ni atoms, which is discussed further in this section. Un-

Understanding the nature and magnitude of charge transfer of $\text{Ni}_{12}\text{P}_5/\text{H}_2\text{O}$ is helpful in understanding its synergistic action between different atoms. When the H_2O molecule is adsorbed to the P atom, the charge state of the molecule changes. From the charge density difference diagram (Figure 6a,b), we can see that there is strong charge accumulation/depletion between the P and O atoms. Because of the high electronegativity, O atoms tend to obtain electrons from adjacent P atoms. Bader charge analysis (Table 3) shows that the charge of a P atom bound to an O atom changes from $-0.18 |e|$ to $0.87 |e|$, among which $-0.53 |e|$ transfer to the O atom and the other electrons transfer to the Ni atoms of Ni_{12}P_5 , which causes the charge of the O atom to decrease from $-1.11 |e|$ to $-1.67 |e|$ (Figure 6c).

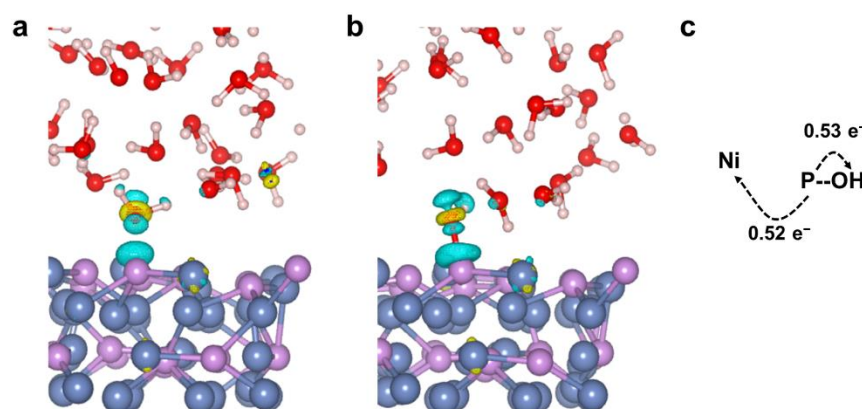


Figure 6. Electron density difference graphs: (a) P^*OH_2 and (b) P^*OH . The accumulation of electron density is indicated by the yellow color, while the depletion of electron density is indicated by the blue color. (c) Direction of electron transfer. The white, red, purple, and blue spheres represent H, O, P, and Ni, respectively.

Table 3. Bader Charge Analysis of $^*\text{H}_2\text{O}$, $^*\text{OH}_2$ and $^*\text{OH} + \text{H}$.

	H_2O				Ni				
	P	O	H^1	H^2	Ni^1	Ni^2	Ni^3	Ni^4	Ni^5
$^*\text{H}_2\text{O}$	-0.18	-1.11	0.55	0.56	0.21	0.21	0.11	0.12	0.08
$^*\text{OH}_2$	0.66	-1.56	0.65	0.60	0.17	0.11	0.12	0.10	0.08
$^*\text{OH} + \text{H}$	0.87	-1.67	0.61	0.59	0.07	0.29	0.06	0.06	0.05

The data listed here are the Bader charges (in the unit $|e|$) of the atoms on the surface; P is the adsorption site of H_2O on the surface, H^1 is the dissociated H atom, H^2 is the H atom in the interaction with $^*\text{OH}$, Ni^1 , Ni^2 , and Ni^3 are the nearest neighbors of P, and Ni^4 and Ni^5 are the next nearest neighbors of P.

Li et al. found that the high oxidation state of Ni active sites, which implies high electron affinity, is conducive to OH^- adsorption and the OER reaction [74]. When the electron in the P atom is transferred to the surrounding Ni atoms, the Ni atoms carry more charge, and thus have low electron affinity, which is not conducive to OH adsorption. On the other hand, the P atoms carries more positive charge, making it easier to adsorb OH. It has been reported that the synergistic effect between atoms can promote charge transfer and accelerate the catalytic reaction [67,75,76]. Therefore, the synergistic action of P and Ni atoms can promote the charge transfer between atoms, and makes P atoms the active sites in OER.

4. Conclusions

In summary, we studied the structural evolution and the adsorption and dissociation of an H_2O molecule on the surface of Ni_{12}P_5 in the aqueous condition using AIMD. The results showed that the H_2O molecule is preferentially adsorbed on the P atom, indicating that the nonmetallic P atom is the active site of the OER reaction. Our simulations show that

the adsorbed H₂O molecule first forms a hydrogen bond with other H₂O molecules, then the hydrogen bond changes from O^a-H ··· O^b to O^a ··· H-O^b, and finally the hydrogen bond breaks and a H⁺ is dissociated. In the OER reaction, the RDS is the formation of the OOH group, and the overpotential of Ni₁₂P₅ is the lowest, thus showing better catalytic activity, which explains the experimental observations. Moreover, we found that the charge of Ni and P sites has a linear relationship with the adsorption energy of OH and O, which can be utilized to optimize OER catalysts. This work provides insights into the OER catalytic performance of nickel phosphide and the design strategy of achieving high OER activity in nickel phosphides.

Supplementary Materials: The following supporting information can be downloaded at: <https://www.mdpi.com/article/10.3390/nano12071130/s1>, Figure S1: (a) Ni₁₂P₅ unit cell. (b)–(f) five lattice planes include (001), (110), (101), (111) and (100), presented by green, purple, orange, cyan and yellow, respectively. Figure S2: The terminated positions on different surfaces before optimization. (a) (001); (b) (110); (c) (101); (d) (111); (e) (100). Violet spheres stand for P atoms and blue spheres stand for Ni atoms. Table S1: k-points setting for different structures. Figure S3: The time evolution of the key bond distances during the AIMD simulation. The black line is the bond distance between the P-O^a. The red line is the bond distance between the H-O^a. The blue line is the bond distance between the H-O^b. H is the dissociated H ion, O^a is the O atom in *OH; O^b is the O atom in another H₂O, and forms O^b-H ··· O^a with H. Figure S4: The time evolution of the key bond distances during the AIMD simulation. The black line is the bond distance between the P-O^a. The red line is the bond distance between the H-O^a. The blue line is the bond distance between the H-O^b. H is the dissociated H ion, O^a is the O atom in *OH; O^b is the O atom in another H₂O, and forms O^b-H ··· O^a with H. Figure S5: The time evolution of Ni-O distances during the AIMD simulation. Figure S6: Geometric configuration of (a) Ni*OH, (b) Ni*O, (c) Ni*OOH, (d) P*OH, (e) P*O and (f) P*OOH adsorption on the Ni₂P (001) surface. Figure S7: Geometric configuration of (a) Ni*OH, (b) Ni*O, (c) Ni*OOH, (d) P*OH, (e) P*O and (f) P*OOH adsorption on the Ni₂P (111) surface. Figure S8: Geometric configuration of (a) Ni*OH, (b) Ni*O, (c) Ni*OOH, (d) P*OH, (e) P*O and (f) P*OOH adsorption on the Ni₁₂P₅ (001) surface. Figure S9: Geometric configuration of (a) Ni*OH, (b) Ni*O, (c) Ni*OOH, (d) P*OH, (e) P*O and (f) P*OOH adsorption on the Ni₁₂P₅ (111) surface. Figure S10: Geometric configuration of (a) Ni*OH, (b) Ni*O, (c) Ni*OOH, (d) P*OH, (e) P*O and (f) P*OOH adsorption on the Ni₅P₂ (001) surface. Figure S11: Geometric configuration of (a) Ni*OH, (b) Ni*O, (c) Ni*OOH, (d) P*OH, (e) P*O and (f) P*OOH adsorption on the Ni₅P₂ (111) surface. Figure S12: Geometric configuration of (a) Ni*OH, (b) Ni*O, (c) Ni*OOH, (d) P*OH, (e) P*O and (f) P*OOH adsorption on the Ni₃P (001) surface. Figure S13: Geometric configuration of (a) Ni*OH, (b) Ni*O, (c) Ni*OOH, (d) P*OH, (e) P*O and (f) P*OOH adsorption on the Ni₃P (111) surface. Table S2: The number of suspended bonds of P and Ni atoms on the exposed surface when establishing different nickel phosphide surfaces. Table S3: Comparison of OER catalytic performance of nickel phosphide in reference. Movie 1: the trajectory of AIMD simulation for the adsorption and dissociation process of H₂O on Ni₁₂P₅ surface. Movie 2: OH moves from Ni to P site. Movie 3: the trajectory of OH on P site. Movie 4: O moves from Ni to P site. Movie 5: the trajectory of O on P site.

Author Contributions: P.Z., Y.X., R.W. and H.Q. conceived and designed the theoretical calculation scheme. P.Z. and Y.X. did the theoretical calculations. P.Z., H.L. and Y.X. wrote and refined the manuscript. H.Q., J.H. and R.W. refined the manuscript. All authors analyzed the data, discussed the results. All authors have read and agreed to the published version of the manuscript.

Funding: This research was funded by the Beijing Natural Science Foundation (Grant No. 2212034), the National Natural Science Foundation of China (Nos. 12034002, 51971025, and 11974041), and the Fundamental Research Funds for the Central Universities (FRF-TP-20-13A).

Acknowledgments: The computing work is supported by USTB MatCom of Beijing Advanced Innovation Center for Materials Genome Engineering.

Conflicts of Interest: The authors declare no conflict of interest.

References

1. Chow, J.; Kopp, R.J.; Portney, P.R. Energy Resources and Global Development. *Science* **2003**, *302*, 1528–1531. [[CrossRef](#)]
2. Chen, G.; Ding, N.; Li, F.; Fan, Y.; Luo, Y.; Li, D.; Meng, Q. Enhancement of photocatalytic H₂ evolution on ZnIn₂S₄ loaded with in-situ photo-deposited MoS₂ under visible light irradiation. *Appl. Catal. B Environ.* **2014**, *160–161*, 614–620. [[CrossRef](#)]
3. Liu, C.; Röder, R.; Zhang, L.; Ren, Z.; Chen, H.; Zhang, Z.; Ronning, C.; Gao, P.-X. Highly efficient visible-light driven photocatalysts: A case of zinc stannate based nanocrystal assemblies. *J. Mater. Chem. A* **2014**, *2*, 4157–4167. [[CrossRef](#)]
4. Wang, C.; Astruc, D. Recent developments of nanocatalyzed liquid-phase hydrogen generation. *Chem. Soc. Rev.* **2021**, *50*, 3437–3484. [[CrossRef](#)]
5. Turner, J.A. A Realizable Renewable Energy Future. *Science* **1999**, *285*, 687–689. [[CrossRef](#)]
6. Subbaraman, R.; Tripkovic, D.; Strmcnik, D.; Chang, K.C.; Uchimura, M.; Paulikas, A.P.; Stamenkovic, V.; Markovic, N.M. Enhancing Hydrogen Evolution Activity in Water Splitting by Tailoring Li⁺-Ni(OH)₂-Pt Interfaces. *Science* **2011**, *334*, 1256–1260. [[CrossRef](#)]
7. Takashima, T.; Hashimoto, K.; Nakamura, R. Inhibition of Charge Disproportionation of MnO₂ Electrocatalysts for Efficient Water Oxidation under Neutral Conditions. *J. Am. Chem. Soc.* **2012**, *134*, 18153–18156. [[CrossRef](#)]
8. Jiang, N.; You, B.; Sheng, M.; Sun, Y. Electrodeposited Cobalt-Phosphorous-Derived Films as Competent Bifunctional Catalysts for Overall Water Splitting. *Angew. Chem. Int. Ed.* **2015**, *54*, 6251–6254. [[CrossRef](#)]
9. Zhang, J.; Zhang, Q.; Feng, X. Support and Interface Effects in Water-Splitting Electrocatalysts. *Adv. Mater.* **2019**, *31*, e1808167. [[CrossRef](#)]
10. Kanan, M.W.; Nocera, D.G. In Situ Formation of an Oxygen-Evolving Catalyst in Neutral Water Containing Phosphate and Co²⁺. *Science* **2008**, *321*, 1072–1075. [[CrossRef](#)]
11. Cherevko, S.; Geiger, S.; Kasian, O.; Kulyk, N.; Grote, J.-P.; Savan, A.; Shrestha, B.R.; Merzlikin, S.; Breitbach, B.; Ludwig, A.; et al. Oxygen and hydrogen evolution reactions on Ru, RuO₂, Ir, and IrO₂ thin film electrodes in acidic and alkaline electrolytes: A comparative study on activity and stability. *Catal. Today* **2016**, *262*, 170–180. [[CrossRef](#)]
12. Danilovic, N.; Subbaraman, R.; Chang, K.C.; Chang, S.H.; Kang, Y.; Snyder, J.; Paulikas, A.P.; Strmcnik, D.; Kim, Y.T.; Myers, D.; et al. Using surface segregation to design stable Ru-Ir oxides for the oxygen evolution reaction in acidic environments. *Angew. Chem. Int. Ed.* **2014**, *53*, 14016–14021. [[CrossRef](#)] [[PubMed](#)]
13. Chen, C.; Kang, Y.; Huo, Z.; Zhu, Z.; Huang, W.; Xin, H.L.; Snyder, J.D.; Li, D.; Herron, J.A.; Mavrikakis, M.; et al. Highly Crystalline Multimetallic Nanoframes with Three-Dimensional Electrocatalytic Surfaces. *Science* **2014**, *343*, 1339–1343. [[CrossRef](#)] [[PubMed](#)]
14. Hong, W.T.; Risch, M.; Stoerzinger, K.A.; Grimaud, A.; Suntivich, J.; Shao-Horn, Y. Toward the rational design of non-precious transition metal oxides for oxygen electrocatalysis. *Energy Environ. Sci.* **2015**, *8*, 1404–1427. [[CrossRef](#)]
15. Yamada, I.; Takamatsu, A.; Asai, K.; Ohzuku, H.; Shirakawa, T.; Uchimura, T.; Kawaguchi, S.; Tsukasaki, H.; Mori, S.; Wada, K.; et al. Synergistically Enhanced Oxygen Evolution Reaction Catalysis for Multielement Transition-Metal Oxides. *ACS Appl. Energy Mater.* **2018**, *1*, 3711–3721. [[CrossRef](#)]
16. Wang, Y.-N.; Yang, Z.-J.; Yang, D.-H.; Zhao, L.; Shi, X.-R.; Yang, G.; Han, B.-H. FeCoP₂ Nanoparticles Embedded in N and P Co-doped Hierarchically Porous Carbon for Efficient Electrocatalytic Water Splitting. *ACS Appl. Mater. Interfaces* **2021**, *13*, 8832–8843. [[CrossRef](#)]
17. Liu, M.; Sun, Z.; Li, S.; Nie, X.; Liu, Y.; Wang, E.; Zhao, Z. Hierarchical superhydrophilic/superaerophobic CoMnP/Ni₂P nanosheet-based microplate arrays for enhanced overall water splitting. *J. Mater. Chem. A* **2021**, *9*, 22129–22139. [[CrossRef](#)]
18. Zhang, Z.; Hao, J.; Yang, W.; Lu, B.; Tang, J. Modifying candle soot with FeP nanoparticles into high-performance and cost-effective catalysts for the electrocatalytic hydrogen evolution reaction. *Nanoscale* **2015**, *7*, 4400–4405. [[CrossRef](#)]
19. Zhang, X.; Shan, A.; Duan, S.; Zhao, H.; Wang, R.; Lau, W.-M. Au@Co₂P core/shell nanoparticles as a nano-electrocatalyst for enhancing the oxygen evolution reaction. *RSC Adv.* **2019**, *9*, 40811–40818. [[CrossRef](#)]
20. Gu, Y.; Chen, S.; Ren, J.; Jia, Y.A.; Chen, C.; Komarneni, S.; Yang, D.; Yao, X. Electronic Structure Tuning in Ni₃FeN/r-GO Aerogel toward Bifunctional Electrocatalyst for Overall Water Splitting. *ACS Nano* **2018**, *12*, 245–253. [[CrossRef](#)]
21. Yang, Y.; Kang, Y.; Zhao, H.; Dai, X.; Cui, M.; Luan, X.; Zhang, X.; Nie, F.; Ren, Z.; Song, W. An Interfacial Electron Transfer on Tetrahedral NiS₂/NiSe₂ Heterocages with Dual-Phase Synergy for Efficiently Triggering the Oxygen Evolution Reaction. *Small* **2020**, *16*, e1905083. [[CrossRef](#)] [[PubMed](#)]
22. Zhang, S.; Li, Y.; Zhu, H.; Lu, S.; Ma, P.; Dong, W.; Duan, F.; Chen, M.; Du, M. Understanding the Role of Nanoscale Heterointerfaces in Core/Shell Structures for Water Splitting: Covalent Bonding Interaction Boosts the Activity of Binary Transition-Metal Sulfides. *ACS Appl. Mater. Interfaces* **2020**, *12*, 6250–6261. [[CrossRef](#)] [[PubMed](#)]
23. Lv, Y.; Duan, S.; Zhu, Y.; Yin, P.; Wang, A.R. Enhanced OER Performances of Au@NiCo₂S₄ Core-Shell Heterostructure. *Nanomaterials* **2020**, *10*, 611. [[CrossRef](#)] [[PubMed](#)]
24. Duan, S.; Lv, Y.; Yin, P.; Zhu, Y.; Wang, R. Constructing the Au-CoNi₂S₄ core-shell heterostructure to promote the catalytic performance for oxygen evolution. *J. Phys. D Appl. Phys.* **2021**, *54*, 425501. [[CrossRef](#)]
25. Yu, Y.; Zhou, J.; Sun, Z. Novel 2D Transition-Metal Carbides: Ultrahigh Performance Electrocatalysts for Overall Water Splitting and Oxygen Reduction. *Adv. Funct. Mater.* **2020**, *30*, 2000570. [[CrossRef](#)]
26. Stern, L.-A.; Feng, L.; Song, F.; Hu, X. Ni₂P as a Janus catalyst for water splitting: The oxygen evolution activity of Ni₂P nanoparticles. *Energy Environ. Sci.* **2015**, *8*, 2347–2351. [[CrossRef](#)]

27. Lai, C.; Liu, X.; Deng, Y.; Yang, H.; Jiang, H.; Xiao, Z.; Liang, T. Rice-shape nanocrystalline Ni₅P₄: A promising bifunctional electrocatalyst for hydrogen evolution reaction and oxygen evolution reaction. *Inorg. Chem. Commun.* **2018**, *97*, 98–102. [[CrossRef](#)]
28. Wang, Q.; Zhang, Z.; Cai, C.; Wang, M.; Zhao, Z.L.; Li, M.; Huang, X.; Han, S.; Zhou, H.; Feng, Z.; et al. Single Iridium Atom Doped Ni₂P Catalyst for Optimal Oxygen Evolution. *J. Am. Chem. Soc.* **2021**, *143*, 13605–13615. [[CrossRef](#)]
29. Riyajuddin, S.; Azmi, K.; Pahuja, M.; Kumar, S.; Maruyama, T.; Bera, C.; Ghosh, K. Super-Hydrophilic Hierarchical Ni-Foam-Graphene-Carbon Nanotubes-Ni₂P-CuP₂ Nano-Architecture as Efficient Electrocatalyst for Overall Water Splitting. *ACS Nano* **2021**, *15*, 5586–5599. [[CrossRef](#)]
30. Zhang, P.; Lu, Y.-R.; Hsu, C.-S.; Xue, H.-G.; Chan, T.-S.; Suen, N.-T.; Chen, H.M. Electronic structure inspired a highly robust electrocatalyst for the oxygen-evolution reaction. *Chem. Commun.* **2020**, *56*, 8071–8074. [[CrossRef](#)]
31. Menezes, P.; Indra, A.; Das, C.; Walter, C.; Göbel, C.; Gutkin, V.; Schmeißer, D.; Driess, M. Uncovering the Nature of Active Species of Nickel Phosphide Catalysts in High-Performance Electrochemical Overall Water Splitting. *ACS Catal.* **2016**, *7*, 103–109. [[CrossRef](#)]
32. Xu, Y.; Duan, S.; Li, H.; Yang, M.; Wang, S.; Wang, X.; Wang, R. Au/Ni₁₂P₅ core/shell single-crystal nanoparticles as oxygen evolution reaction catalyst. *Nano Res.* **2017**, *10*, 3103–3112. [[CrossRef](#)]
33. Sun, H.; Min, Y.; Yang, W.; Lian, Y.; Lin, L.; Feng, K.; Deng, Z.; Chen, M.; Zhong, J.; Xu, L.; et al. Morphological and Electronic Tuning of Ni₂P through Iron Doping toward Highly Efficient Water Splitting. *ACS Catal.* **2019**, *9*, 8882–8892. [[CrossRef](#)]
34. Zhang, W.-Z.; Chen, G.-Y.; Zhao, J.; Liang, J.-C.; Sun, L.-F.; Liu, G.-F.; Ji, B.-W.; Yan, X.-Y.; Zhang, J.-R. Self-growth Ni₂P nanosheet arrays with cationic vacancy defects as a highly efficient bifunctional electrocatalyst for overall water splitting. *J. Colloid Interface Sci.* **2020**, *561*, 638–646. [[CrossRef](#)]
35. Yan, H.; Xie, Y.; Wu, A.; Cai, Z.; Wang, L.; Tian, C.; Zhang, X.; Fu, H. Anion-Modulated HER and OER Activities of 3D Ni-V-Based Interstitial Compound Heterojunctions for High-Efficiency and Stable Overall Water Splitting. *Adv. Mater.* **2019**, *31*, e1901174. [[CrossRef](#)]
36. Wen, S.; Chen, G.; Chen, W.; Li, M.; Ouyang, B.; Wang, X.; Chen, D.; Gong, T.; Zhang, X.; Huang, J.; et al. Nb-doped layered FeNi phosphide nanosheets for highly efficient overall water splitting under high current densities. *J. Mater. Chem. A* **2021**, *9*, 9918–9926. [[CrossRef](#)]
37. Rossmeisl, J.; Logadottir, A.; Nørskov, J.K. Electrolysis of water on (oxidized) metal surfaces. *Chem. Phys.* **2005**, *319*, 178–184. [[CrossRef](#)]
38. Rossmeisl, J.; Qu, Z.W.; Zhu, H.; Kroes, G.J.; Nørskov, J.K. Electrolysis of water on oxide surfaces. *J. Electroanal. Chem.* **2007**, *607*, 83–89. [[CrossRef](#)]
39. Man, I.C.; Su, H.-Y.; Calle-Vallejo, F.; Hansen, H.A.; Martínez, J.I.; Inoglu, N.G.; Kitchin, J.; Jaramillo, T.F.; Nørskov, J.K.; Rossmeisl, J. Universality in Oxygen Evolution Electrocatalysis on Oxide Surfaces. *ChemCatChem* **2011**, *3*, 1159–1165. [[CrossRef](#)]
40. Zhang, J.; Wang, T.; Pohl, D.; Rellinghaus, B.; Dong, R.; Liu, S.; Zhuang, X.; Feng, X. Interface Engineering of MoS₂/Ni₃S₂ Heterostructures for Highly Enhanced Electrochemical Overall-Water-Splitting Activity. *Angew. Chem. Int. Ed.* **2016**, *55*, 6702–6707. [[CrossRef](#)]
41. Skelton, A.A.; Fenter, P.; Kubicki, J.D.; Wesolowski, D.J.; Cummings, P.T. Simulations of the Quartz(10 $\bar{1}$ 1)/Water Interface: A Comparison of Classical Force Fields, Ab Initio Molecular Dynamics, and X-ray Reflectivity Experiments. *J. Phys. Chem. C* **2011**, *115*, 2076–2088. [[CrossRef](#)]
42. Hassanali, A.A.; Cuny, J.; Verdolino, V.; Parrinello, M. Aqueous solutions: State of the art in ab initio molecular dynamics. *Philos. Trans. R. Soc. A Math. Phys. Eng. Sci.* **2014**, *372*, 20120482. [[CrossRef](#)] [[PubMed](#)]
43. Li, C.-Y.; Le, J.-B.; Wang, Y.-H.; Chen, S.; Yang, Z.-L.; Li, J.-F.; Cheng, J.; Tian, Z.-Q. In situ probing electrified interfacial water structures at atomically flat surfaces. *Nat. Mater.* **2019**, *18*, 697–701. [[CrossRef](#)]
44. Réocreux, R.; Jiang, T.; Iannuzzi, M.; Michel, C.; Sautet, P. Structuration and Dynamics of Interfacial Liquid Water at Hydrated γ -Alumina Determined by ab Initio Molecular Simulations: Implications for Nanoparticle Stability. *ACS Appl. Nano Mater.* **2017**, *1*, 191–199. [[CrossRef](#)]
45. Kresse, G.; Furthmüller, J. Efficiency of ab-initio total energy calculations for metals and semiconductors using a plane-wave basis set. *Comput. Mater. Sci.* **1996**, *6*, 15–50. [[CrossRef](#)]
46. Kresse, G.; Furthmüller, J. Efficient iterative schemes for ab initio total-energy calculations using a plane-wave basis set. *Phys. Rev. B* **1996**, *54*, 11169–11186. [[CrossRef](#)]
47. Perdew, J.P.; Chevary, J.A.; Vosko, S.H.; Jackson, K.A.; Pederson, M.R.; Singh, D.J.; Fiolhais, C. Atoms, molecules, solids, and surfaces: Applications of the generalized gradient approximation for exchange and correlation. *Phys. Rev. B* **1992**, *46*, 6671–6687. [[CrossRef](#)]
48. Blochl, P.E. Projector augmented-wave method. *Phys. Rev. B* **1994**, *50*, 17953–17979. [[CrossRef](#)]
49. Nørskov, J.K.; Rossmeisl, J.; Logadottir, A.; Lindqvist, L.; Kitchin, J.R.; Bligaard, T.; Jónsson, H. Origin of the Overpotential for Oxygen Reduction at a Fuel-Cell Cathode. *J. Phys. Chem. B* **2004**, *108*, 17886–17892. [[CrossRef](#)]
50. Wang, V.; Xu, N.; Liu, J.-C.; Tang, G.; Geng, W.-T. VASPKIT: A user-friendly interface facilitating high-throughput computing and analysis using VASP code. *Comput. Phys. Commun.* **2021**, *267*, 108033. [[CrossRef](#)]
51. Hoover, W.G. Canonical dynamics: Equilibrium phase-space distributions. *Phys. Rev. A* **1985**, *31*, 1695–1697. [[CrossRef](#)] [[PubMed](#)]
52. VandeVondele, J.; Krack, M.; Mohamed, F.; Parrinello, M.; Chassaing, T.; Hutter, J. Quickstep: Fast and accurate density functional calculations using a mixed Gaussian and plane waves approach. *Comput. Phys. Commun.* **2005**, *167*, 103–128. [[CrossRef](#)]

53. VandeVondele, J.; Hutter, J. Gaussian basis sets for accurate calculations on molecular systems in gas and condensed phases. *J. Chem. Phys.* **2007**, *127*, 114105. [[CrossRef](#)]
54. Goedecker, S.; Teter, M.; Hutter, J. Separable dual-space Gaussian pseudopotentials. *Phys. Rev. B* **1996**, *54*, 1703–1710. [[CrossRef](#)] [[PubMed](#)]
55. Hartwigsen, C.; Goedecker, S.; Hutter, J. Relativistic separable dual-space Gaussian pseudopotentials from H to Rn. *Phys. Rev. B* **1998**, *58*, 3641–3662. [[CrossRef](#)]
56. Perdew, J.P.; Burke, K.; Ernzerhof, M. Generalized gradient approximation made simple. *Phys. Rev. Lett.* **1996**, *77*, 3865–3868. [[CrossRef](#)] [[PubMed](#)]
57. Grimme, S.; Antony, J.; Ehrlich, S.; Krieg, H. A consistent and accurate ab initio parametrization of density functional dispersion correction (DFT-D) for the 94 elements H–Pu. *J. Chem. Phys.* **2010**, *132*, 154104–154119. [[CrossRef](#)]
58. Reuter, K.; Scheffler, M. Composition, structure, and stability of RuO₂(110) as a function of oxygen pressure. *Phys. Rev. B* **2001**, *65*, 035406. [[CrossRef](#)]
59. Wexler, R.B.; Martirez, J.M.P.; Rappe, A.M. Stable Phosphorus-Enriched (0001) Surfaces of Nickel Phosphides. *Chem. Mater.* **2016**, *28*, 5365–5372. [[CrossRef](#)]
60. Loh, Z.-H.; Doumy, G.; Arnold, C.; Kjellsson, L.; Southworth, S.H.; Al Haddad, A.; Kumagai, Y.; Tu, M.-F.; Ho, P.J.; March, A.M.; et al. Observation of the fastest chemical processes in the radiolysis of water. *Science* **2020**, *367*, 179–182. [[CrossRef](#)]
61. Emamian, S.; Lu, T.; Kruse, H.; Emamian, H. Exploring Nature and Predicting Strength of Hydrogen Bonds: A Correlation Analysis between Atoms-in-Molecules Descriptors, Binding Energies, and Energy Components of Symmetry-Adapted Perturbation Theory. *J. Comput. Chem.* **2019**, *40*, 2868–2881. [[CrossRef](#)] [[PubMed](#)]
62. Wang, S.; MacKay, L.; Lamoureux, G. Development of Semiempirical Models for Proton Transfer Reactions in Water. *J. Chem. Theory Comput.* **2014**, *10*, 2881–2890. [[CrossRef](#)] [[PubMed](#)]
63. Pezeshki, S.; Lin, H. Adaptive-Partitioning QM/MM for Molecular Dynamics Simulations: 4. Proton Hopping in Bulk Water. *J. Chem. Theory Comput.* **2015**, *11*, 2398–2411. [[CrossRef](#)] [[PubMed](#)]
64. Xu, H.; Zhu, J.; Wang, P.; Chen, D.; Zhang, C.; Xiao, M.; Ma, Q.; Bai, H.; Qin, R.; Ma, J.; et al. Fe–Co–P multi-heterostructure arrays for efficient electrocatalytic water splitting. *J. Mater. Chem. A* **2021**, *9*, 24677–24685. [[CrossRef](#)]
65. Légaré, M.-A.; Bélanger-Chabot, G.; Dewhurst, R.D.; Welz, E.; Krummenacher, I.; Engels, B.; Braunschweig, H. Nitrogen fixation and reduction at boron. *Science* **2018**, *359*, 896–900. [[CrossRef](#)]
66. Deng, J.; Li, H.; Xiao, J.; Tu, Y.; Deng, D.; Yang, H.; Tian, H.; Li, J.; Ren, P.; Bao, X. Triggering the electrocatalytic hydrogen evolution activity of the inert two-dimensional MoS₂ surface via single-atom metal doping. *Energy Environ. Sci.* **2015**, *8*, 1594–1601. [[CrossRef](#)]
67. Fei, H.; Dong, J.; Feng, Y.; Allen, C.S.; Wan, C.; Voloskiy, B.; Li, M.; Zhao, Z.; Wang, Y.; Sun, H.; et al. General synthesis and definitive structural identification of MN₄C₄ single-atom catalysts with tunable electrocatalytic activities. *Nat. Catal.* **2018**, *1*, 63–72. [[CrossRef](#)]
68. Zhang, W.; Fu, Q.; Luo, Q.; Sheng, L.; Yang, J. Understanding Single-Atom Catalysis in View of Theory. *JACS Au* **2021**, *1*, 2130–2145. [[CrossRef](#)]
69. Dong, C.; Li, Y.; Cheng, D.; Zhang, M.; Liu, J.; Wang, Y.-G.; Xiao, D.; Ma, D. Supported Metal Clusters: Fabrication and Application in Heterogeneous Catalysis. *ACS Catal.* **2020**, *10*, 11011–11045. [[CrossRef](#)]
70. Wang, H.; Zhang, X.; Yin, F.; Chu, W.; Chen, B. Coordinately unsaturated metal–organic framework as an unpyrolyzed bifunctional electrocatalyst for oxygen reduction and evolution reactions. *J. Mater. Chem. A* **2020**, *8*, 22111–22123. [[CrossRef](#)]
71. Shah, K.; Dai, R.; Mateen, M.; Hassan, Z.; Zhuang, Z.; Liu, C.; Israr, M.; Cheong, W.-C.; Hu, B.; Tu, R.; et al. Cobalt Single Atom Incorporated in Ruthenium Oxide Sphere: A Robust Bifunctional Electrocatalyst for HER and OER. *Angew. Chem. Int. Ed.* **2022**, *61*, e202114951. [[CrossRef](#)] [[PubMed](#)]
72. Li, C.; Zhao, J.; Xie, L.; Wu, J.; Ren, Q.; Wang, Y.; Li, G. Surface-Adsorbed Carboxylate Ligands on Layered Double Hydroxides/Metal–Organic Frameworks Promote the Electrocatalytic Oxygen Evolution Reaction. *Angew. Chem. Int. Ed.* **2021**, *60*, 18129–18137. [[CrossRef](#)]
73. Wang, T.; Chen, H.; Yang, Z.; Liang, J.; Dai, S. High-Entropy Perovskite Fluorides: A New Platform for Oxygen Evolution Catalysis. *J. Am. Chem. Soc.* **2020**, *142*, 4550–4554. [[CrossRef](#)] [[PubMed](#)]
74. Zhao, Q.; Yang, J.; Liu, M.; Wang, R.; Zhang, G.; Wang, H.; Tang, H.; Liu, C.; Mei, Z.; Chen, H.; et al. Tuning Electronic Push/Pull of Ni-Based Hydroxides To Enhance Hydrogen and Oxygen Evolution Reactions for Water Splitting. *ACS Catal.* **2018**, *8*, 5621–5629. [[CrossRef](#)]
75. Li, X.; Wang, X.; Zhou, J.; Han, L.; Sun, C.; Wang, Q.; Su, Z. Ternary hybrids as efficient bifunctional electrocatalysts derived from bimetallic metal–organic-frameworks for overall water splitting. *J. Mater. Chem. A* **2018**, *6*, 5789–5796. [[CrossRef](#)]
76. Chu, S.; Sun, H.; Chen, G.; Chen, Y.; Zhou, W.; Shao, Z. Rationally designed Water-Insertable Layered Oxides with Synergistic Effect of Transition-Metal Elements for High-Performance Oxygen Evolution Reaction. *ACS Appl. Mater. Interfaces* **2019**, *11*, 25227–25235. [[CrossRef](#)]